https://doi.org/10.5194/egusphere-2026-2943
Preprint. Discussion started: 23 June 2026

Spectral Signatures of Zenith Sky Radiances from Surface-Based Sky Radiometers: Implications for Clear- and Cloudy-Sky Detection

Pradeep Khatri[1], Hitoshi Irie[2], Hiroshi Kobayashi[3], Isamu Morino[4], Yoshitaka Jin[4], Tadahiro Hayasaka[5], Hironobu Iwabuchi[6], Tamio Takamura[2], and Yoshiki Takayama[7]

[1]Department of Green Technology, Faculty of Science and Engineering, Soka University, Hachioji, Tokyo, Japan
[2]Center for Environmental Remote Sensing, Chiba University, Chiba, Japan
[3]Department of Environmental Sciences, Faculty of Life and Environmental Sciences, University of Yamanashi, Yamanashi, Japan
[4]National Institute for Environmental Studies, Tsukuba, Japan
[5]Graduate School of Science, Tohoku University, Sendai, Japan
[6]Center for Atmospheric and Oceanic Studies, Tohoku University, Sendai, Japan
[7] Graduate School of Environment and Information Sciences, Yokohama National University, Yokohama, Japan

Correspondence to: Pradeep Khatri (pradeep@soka.ac.jp)

Abstract. Accurate identification of clear- and cloudy-sky conditions is essential for reliable aerosol and cloud retrievals from ground-based remote sensing observations. This study investigates the spectral characteristics of zenith radiances measured by SKYNET sky radiometers and evaluates their potential for distinguishing clear- and cloudy-sky conditions based on wavelength dependence. Analyses of normalized spectral zenith radiances at multiple sites representing diverse atmospheric environments, including urban, maritime, tropical continental, and polar regions, revealed systematic differences between clear- and cloudy-sky conditions identified using quality-controlled MODIS cloud mask products. The spectral slope derived from the logarithmic contrast between zenith radiances at 0.400 and 0.675 µm showed strong sensitivity to cloudy-sky conditions but limited capability for detecting clear-sky conditions. In contrast, slopes based on the 0.500 and 0.675 µm and 0.400 and 0.675 µm wavelength pairs exhibited more balanced detection performance for both clear- and cloudy-sky conditions. Based on detailed analyses of the dependence of these slope values on solar geometry, aerosol properties, and cloud properties, together with classification scores evaluated against MODIS cloud mask data, this study proposes a simple, efficient, and easy-to-use sky-state detection criterion that classifies observations into clear, cloudy, and undetermined categories. Independent validation using collocated direct normal irradiance measurements confirmed the physical consistency of the slope-based classification. Further comparison with the standard cloud-screening procedure showed very good agreement in clear-sky aerosol data extracted using the newly developed criterion across diverse atmospheric environments. Overall, these results demonstrate that spectral zenith radiances provide a simple and physically interpretable basis for clear- and cloudy-sky detection. Incorporating such spectral diagnostics into ground-based radiometric networks can improve cloud screening and enhance the reliability of long-term aerosol and cloud climatological analyses.

1 Introduction

Aerosols and clouds play fundamental roles in the Earth's radiation budget and environmental systems by regulating the balance between incoming solar radiation and outgoing terrestrial radiation, while simultaneously influencing atmospheric thermodynamic structure and hydrological processes (IPCC 2023). Through scattering and absorption of solar and terrestrial radiation, aerosols modify atmospheric heating rates and surface energy availability, whereas clouds exert strong radiative forcing by reflecting shortwave radiation and trapping longwave radiation. These processes directly affect atmospheric circulation, precipitation formation, and climate feedback mechanisms. Consequently, accurate characterization of aerosols and clouds is essential for understanding the Earth system and reducing uncertainties in climate projections.

https://doi.org/10.5194/egusphere-2026-2943
Preprint. Discussion started: 23 June 2026

Advances in remote sensing technologies over the past decades have substantially improved the capability to observe atmospheric constituents from both satellite platforms and ground-based systems. Satellite observations provide extensive spatial coverage and enable global monitoring of aerosol and cloud distributions, while ground-based measurements offer high temporal resolution that are often difficult to obtain from spaceborne sensors. Within such observational frameworks, ground-based remote sensing instruments such as the SKYNET sky radiometer network (Nakajima et al., 2020) have proven particularly valuable. SKYNET sky radiometers provide high-quality spectral direct solar irradiance and diffuse radiance measurements that enable retrievals of key aerosol properties including aerosol optical thickness, single scattering albedo, and particle size distributions (Hashimoto et al. 2012; Nakajima et al. 2020). In addition to aerosol observations, recent methodological developments have demonstrated that these instruments can also be used to retrieve cloud optical properties such as cloud optical depth and cloud particle effective radius from spectral zenith radiance measurements (Khatri et al. 2018, 2019, 2022). Because the measurements are obtained continuously with high temporal resolution, sky radiometers provide valuable long-term datasets that complement satellite retrievals and serve as high-quality reference observations for validation and climatological analyses.

Such datasets have been widely used in studies aimed at improving the understanding of aerosol–cloud interactions, evaluating satellite products, and examining regional and long-term atmospheric variability (Bi et al., 2014; Damiani et al., 2019; Irie et al., 2019; Khatri et al., 2010, 2014a, 2018, 2022; Ningombam et al., 2024; Wang et al., 2014). In addition, under clear-sky conditions, the sky radiometers can provide information on atmospheric gases such as water vapor (Campanelli et al., 2014) and ozone (Khatri et al. 2014b). These capabilities demonstrate that sky radiometer observations constitute a versatile dataset for investigating multiple atmospheric components within a unified observational framework.

Given these diverse applications, reliable discrimination between clear-sky and cloudy-sky conditions is a fundamental prerequisite for maximizing the utility of SKYNET observations. Many aerosol retrieval algorithms assume cloud-free conditions because clouds strongly perturb the radiative field and can introduce substantial biases in aerosol optical property retrievals. Similarly, atmospheric absorbing gases retrieval methods relying on spectral absorption features require uncontaminated clear-sky measurements to ensure accuracy. The sky-condition classification is therefore essential for maintaining data quality, improving retrieval reliability, and strengthening the credibility of satellite validation and model evaluation studies that rely on ground-based reference observations.

Despite its importance, a discrimination between clear and cloudy skies remains challenging in practical observations. Thin cirrus clouds, subvisual cloud layers, and rapidly evolving cloud fields can produce radiative signatures that resemble clear-sky conditions when evaluated using traditional screening approaches. In addition, atmospheric conditions characterized by high aerosol loading—such as mineral dust outbreaks, biomass-burning plumes, or pollution events—can significantly increase atmospheric turbidity. Under such conditions, irradiance variability or other statistical indicators used for cloud screening may incorrectly classify aerosol-rich but cloud-free skies as cloudy. These factors introduce uncertainties in sky-condition classification and can degrade the quality of derived atmospheric products.

Several cloud detection approaches have been proposed to address this problem. For example, the method developed by Khatri and Takamura (2009), uses the temporal variability of global irradiance, wavelength dependency behaviour of aerosols, and statistical approach to identify cloud contamination, while Song et al. (2014) uses somewhat different statistical approach. Although these approaches have proven useful in many applications, they may exhibit limitations under conditions characterized by complex aerosol loading or rapidly evolving cloud fields. Consequently, there remains a need for a simple physically interpretable method for discriminating between clear and cloudy sky conditions using readily available observational parameters.

To address these issues, it is necessary to investigate observational quantities that exhibit direct sensitivity to cloud scattering processes. Among them, spectral zenith radiances measured by sky radiometers provide particularly valuable information for sky-condition discrimination. Zenith radiances are directly influenced by scattering from cloud particles within the instrument's instantaneous field of view, making them sensitive indicators of cloud presence even when cloud optical thickness is relatively small (Khatri et al., 2018, 2019, 2022). Because cloud particles typically produce stronger and spectrally distinct scattering signals compared with aerosols, zenith radiance measurements can reveal subtle cloud contamination that may not be captured by irradiance-based screening methods or purely statistical approaches. Despite this strong physical sensitivity to cloud scattering, zenith radiance observations have not yet been fully exploited in operational cloud-screening procedures for sky radiometer datasets. Most existing screening algorithms rely primarily on irradiance variability or derived statistical indicators rather than directly utilizing the spectral information contained in zenith radiance measurements. This gap suggests

https://doi.org/10.5194/egusphere-2026-2943
Preprint. Discussion started: 23 June 2026

that additional investigation into the potential of zenith radiances could lead to improved methods for sky-condition classification.

The present study aims to systematically evaluate the capability of spectral zenith radiance measurements for discriminating between clear and cloudy sky conditions. By examining the spectral characteristics of zenith radiances under different atmospheric states, the study seeks to establish physically based criterion for identifying cloud contamination in sky radiometer observations. The resulting methodology can be applied either independently or in combination with existing cloud-screening techniques to enhance the reliability and quality of atmospheric retrievals derived from SKYNET measurements.

Beyond improving SKYNET data processing, the findings of this study may also provide useful insights for other ground-based aerosol monitoring networks. In particular, networks such as AERONET (Holben et al., 1998) , which also rely on ground-based radiometric observations for aerosol characterization, may benefit from improved sky-condition screening approaches informed by the radiative behaviour of spectral measurements. By strengthening the ability to distinguish between aerosol-dominated and cloud-contaminated observations, such improvements would contribute to more accurate aerosol climatology, more reliable satellite validation efforts, and a deeper understanding of aerosol–cloud–radiation interactions in the Earth's atmosphere.

2 Observation Sites and Data

This study analyses observation data from eight SKYNET sites, including Chiba, Cape Hedo, Fukue, Miyako, Sendai, Burgos, Syowa, and Ny-Ålesund, which collectively cover a wide range of atmospheric conditions across mid-latitude, tropical, and polar environments (Table 1). As summarized in Table 1, Chiba represents an urban–coastal polluted environment influenced by anthropogenic emissions from Tokyo metropolitan emissions and marine air from the Pacific, with episodic long-range transport of continental aerosols from East Asia (Xue et al., 2021). Cape Hedo is located on Okinawa Island and is often considered a marine background site in the western Pacific, although it is periodically affected by long-range transport of Asian dust and anthropogenic aerosols (Khatri et al., 2010). Fukue Island, situated in the East China Sea region, represents a continental outflow receptor site that receives transported aerosols from East Asia mixed with marine air masses (Khatri et al., 2014a). Similar to Hedo, Miyako represents a mid-latitude maritime environment with generally clean oceanic air masses but episodic influence from long-range transport of continental aerosols (Dim et al., 2013). Sendai is a mid-latitude coastal site influenced by regional urban emissions and seasonal continental transport from East Asia (Shiobara et al., 1991). Burgos in the northern Philippines represents a tropical maritime environment dominated by Pacific trade winds with occasional influence from transported aerosols from East and Southeast Asia (Bagtasa et al., 2018). In addition, two polar sites are included: Syowa Station in Antarctica, representing a polar pristine environment with extremely low aerosol loading and occasional long-range transport from midlatitudes and low latitudes (Hara et al., 2025); and Ny-Ålesund in the high Arctic, which represents an Arctic background environment influenced by seasonal long-range transport of pollution known as Arctic haze emitted from midlatitudes (Pasquier et al., 2022). The data analyses periods in this study vary among the sites depending on data availability, extending from January 2010 up to December 2024 (Table 1).

The study utilized observational data from multiple complementary sources, including a sky radiometer (Model: POM-02, PREDE Co., Ltd.), the Moderate Resolution Imaging Spectroradiometer (MODIS), and ground-based direct solar irradiance measurements obtained using a pyrheliometer.

From the sky radiometer, two categories of measurements were employed. First, unprocessed spectral zenith radiances at wavelengths with negligible absorption by atmospheric gases — 0.340, 0.380, 0.400, 0.500, 0.675, 0.870, and 1.020 μm — were used. The direct and almucantar radiances observed at these wavelengths are commonly used in SKYNET for aerosol observations. The zenith radiances observed at these wavelenghts provide valuable information about sky brightness and atmospheric scattering characteristics under both clear- and cloudy-sky conditions.

Second, quality-controlled aerosol optical thickness (AOT) values at wavelengths of 0.400, 0.500, and 0.870 μm were used. These values were processed using skyrad.pack inversion software (Hashimoto et al., 2012) and cloud-screening algorithm (Khatri and Takamura, 2009) both of which are incorporated in SR-CEReS (Sky Radiometer–Center for Environmental Remote Sensing) processing package. The data are publicly available through the SKYNET data archive (http://atmos3.cr.chiba-u.jp/skynet/).

https://doi.org/10.5194/egusphere-2026-2943
Preprint. Discussion started: 23 June 2026

Table 1. Observation locations, representative airmass types, and study periods

Study Location	Representative Air Mass Type	Study Period
Chiba (Japan) (35.625°N, 140.104°E)	Urban–coastal air mass influenced by Tokyo emissions, marine air, and episodic East Asian aerosol transport.	January, 2010 ~ December, 2024
Cape Hedo (26.867°N, 128.248°E)	Marine background air mass influenced by long-range transport from East Asia	February, 2010 ~ February, 2021
Fukue (Japan) (32.752°N, 128.682°E)	Continental outflow with marine mixing	January, 2010 ~ July, 2019
Miayko (Japan) (24.737°N, 125.327°E)	Maritime background air mass with episodic Asian dust and pollution transport	August, 2017 ~ November, 2020
Sendai (Japan) (38.26°N, 140.84°E)	Mid-latitude coastal air mass influenced by continental and marine sources	July, 2018 ~ December, 2024
Burgos (Philippines) (18.533°N, 120.650°E)	Maritime tropical air mass with occasional long-range transport	March, 2018 ~ December, 2024
Syowa (Antrarctica) (-69.006S,°N, 39.590°E)	Polar background (pristine) air mass with extremely low aerosol loading and occasional long-range transport.	February,2009~December, 2021
Ny-Ålesund (Norway) (78.929°N, 11.861°E)	Arctic background air mass with seasonal long-range transport infuence.	March,2011~ September, 2018

Satellite-based cloud information and cloud optical properties were obtained from MODIS Level-2 cloud mask and cloud property products. Specifically, the MOD35_L2 product from the Terra satellite and the MYD35_L2 product from the Aqua satellite were used for cloud mask information, while cloud optical properties were obtained from the MOD06_L2 and MYD06_L2 products corresponding to Terra and Aqua satellites, respectively. The MODIS cloud mask products provide pixel-level cloud detection using a series of multispectral threshold tests that analyze radiances measured in visible, near-infrared, and thermal infrared channels. The cloud mask algorithm classifies each pixel into categories such as clear, probably clear, probably cloudy, and cloudy based on spectral characteristics and spatial consistency tests. The fundamental framework of this cloud detection approach is described by Ackerman et al., (1998). The MODIS cloud optical property products provide retrieved cloud optical thickness, cloud effective radius, and related cloud microphysical parameters using multispectral reflectance measurements, primarily from visible, near-infrared, and shortwave-infrared bands. These retrievals are based on the bispectral method, in which cloud optical thickness is mainly constrained by visible-band reflectance, while cloud particle effective radius is inferred from absorbing near-infrared or shortwave-infrared channels(Platnick et al., 2017; Nakajima and King, 1990). Both cloud mask and cloud property products have a nominal spatial resolution of approximately 1 km at nadir.

In addition to the sky radiometer and satellite observations, direct normal irradiance (DNI) measurements were also utilized where available. These measurements were obtained using a pyrheliometer manufactured by Kipp & Zonen, which measures the solar irradiance received directly from the sun within a narrow field of view aligned with the solar disk. Pyrheliometers provide highly accurate measurements of DNI and are widely used in atmospheric radiation studies as well as solar energy applications. DNI observations are particularly useful for identifying clear-sky conditions and for assessing the influence of clouds and aerosols on direct solar radiation reaching the Earth's surface.

3 Methodology

To investigate the spectral characteristics of zenith sky radiances under clear- and cloudy-sky conditions, sky radiometer–observed zenith radiance measurements were temporally collocated with MODIS overpass times by selecting observations with an absolute time difference of less than 5 minutes, noting that zenith sky radiances are measured at time interval of 10 minutes. Based on this temporal collocation, the corresponding spectral zenith radiances were categorized into two groups:

https://doi.org/10.5194/egusphere-2026-2943
Preprint. Discussion started: 23 June 2026

confidently clear and confidently cloudy conditions as identified by the MODIS cloud mask product. The MODIS cloud mask data used in this study were quality-controlled using strict spatial and quality-assurance criteria. For each ground-based observation, the nine MODIS pixels closest to the observation site, corresponding to a 3 × 3 pixel area cantered the observation site, were extracted. Only cases for which all nine closest pixels were available and the minimum distance between the observation site and the nearest MODIS pixel was less than 1 km were retained. A scene was classified as confidently clear only when all nine pixels were identified as confident clear with a MODIS quality-assurance level of 6 or higher. Similarly, a scene was classified as confidently cloudy only when all nine pixels were identified as cloudy with a MODIS quality-assurance level of 6 or higher. This strict screening criterion can substantially reduce uncertainties associated with cloud-edge contamination, geolocation mismatch, and mixed clear–cloudy scenes. However, some uncertainties may still remain, particularly under broken-cloud conditions, where the spatial distribution of clouds can change rapidly within the MODIS pixel area and during the short time interval between satellite overpass and ground-based observation. Therefore, although the applied criteria may provide a basis for separating clear and cloudy cases as rigorously as possible, possible residual mismatches between the satellite-derived cloud mask and the actual sky condition observed by the sky radiometer cannot be completely eliminated.

For each observation time, the radiance spectrum was normalized by its maximum value to reduce the influence of absolute radiance magnitude and to emphasize the spectral shape of the zenith radiance. The normalized radiance spectra were then analysed separately for the clear-sky and cloudy-sky groups. In particular, the median values of the normalized radiance spectra at each wavelength were calculated in order to characterize the typical spectral features associated with clear and cloudy atmospheric conditions.

To further quantify the spectral dependence of zenith radiances, slope values were calculated for all possible wavelength pairs for each observation time using the following equation:

$$\mathrm{Slope}(\lambda_1, \lambda_2) = \ln(I\lambda_1 / I\lambda_2) / \ln(\lambda_1 / \lambda_2), \quad (1)$$

where $I\lambda_1$ and $I\lambda_2$ represent the zenith sky radiances at wavelengths λ_1 and λ_2, respectively. This formulation describes the spectral gradient of zenith sky radiance between two wavelengths and provides a quantitative measure of the spectral dependence of scattered radiation in the atmosphere. The slope values effectively capture differences in the spectral shape of zenith sky radiances, which are influenced by atmospheric scattering processes associated with aerosols, molecules, and clouds.

By analyzing the slope values derived from Eq. (1) for the grouped clear- and cloudy-sky datasets, threshold-based criterion was established to discriminate between clear and cloudy conditions. In addition, the collocated aerosol data and MODIS Level-2 cloud property data were statistically analyzed to examine the behavior of these spectral slopes under varying atmospheric conditions while developing criteria for detecting sky condition.

The resulting classification of clear and cloudy sky conditions was evaluated using collocated direct normal irradiance (DNI) measurements, applying a temporal matching criterion of less than 2.5 minutes. DNI is highly sensitive to the presence of clouds; under clear-sky conditions, DNI typically exhibits relatively high values because direct solar radiation reaches the surface without obstruction. In contrast, the presence of clouds significantly attenuates the direct solar beam, leading to substantially reduced DNI values. Therefore, DNI measurements provide an independent observational reference for assessing the reliability and robustness of the proposed classification approach.

Additional validation was conducted by comparing aerosol optical thickness (AOT) at 0.5 μm and the Ångström exponent (AE) obtained for clear-sky cases identified by the proposed slope-based method with those derived using the cloud-screening algorithm of Khatri and Takamura (2009). The Ångström exponent, which characterizes the spectral dependence of aerosol optical thickness and is commonly used as an indicator of aerosol particle size, was calculated as

$$\mathrm{AE} = -\ln(\mathrm{AOT}_{0.40} / \mathrm{AOT}_{0.87}) / \ln(0.400/ 0.870), \quad (2)$$

where $\mathrm{AOT}_{0.40}$ and $\mathrm{AOT}_{0.87}$ represent aerosol optical thickness at wavelengths of 0.400 μm and 0.870 μm, respectively. This comparison provides an additional consistency check by examining whether the aerosol optical properties retrieved under the clear-sky conditions identified by the proposed slope-based method are physically reasonable and consistent with those obtained using an established cloud-screening algorithm.

https://doi.org/10.5194/egusphere-2026-2943
Preprint. Discussion started: 23 June 2026

4 Results and Discussion

4.1 Spectral Signatures of Zenith Radiance Under Clear and Cloudy Skies

4.1.1 General Features

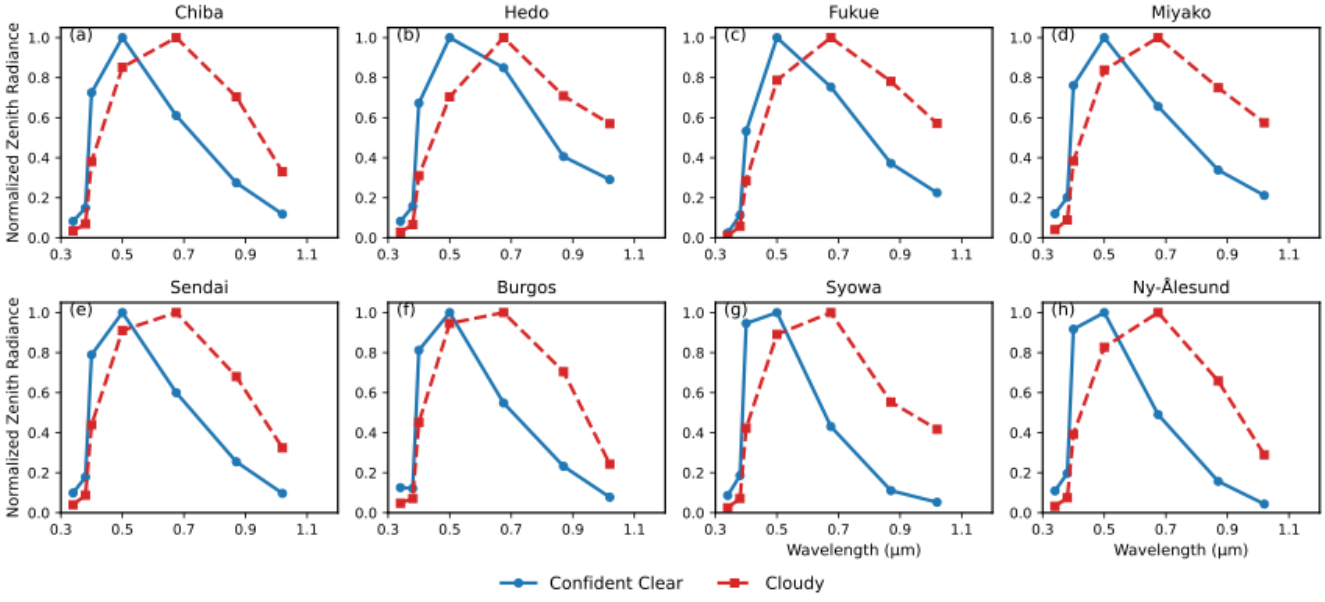

Figure 1. Median normalized spectral zenith radiance under cloudy and confidently clear sky conditions at (a) Chiba, (b) Hedo, (c) Fukue, (d) Miyako, (e)Sendai, (f) Burgos, (g) Syowa, and (h) Ny-Ålesund. Zenith radiances were normalized by the maximum value within each observation and averaged separately for MODIS-identified cloudy and confidently clear cases.

Figure 1 presents the median normalized spectral zenith radiances under confidently clear and cloudy sky conditions at eight selected SKYNET sites. For each observation, the radiance spectrum was normalized by its maximum value before calculating the median spectrum. Therefore, the figure emphasizes differences in spectral shape and relative spectral distribution rather than absolute radiance magnitude.

Across all sites, the spectral curves under cloudy and clear conditions exhibit systematically different patterns. Under cloudy conditions, the normalized spectra appear relatively flat across the visible wavelength range (approximately 0.400–0.870 μm), indicating weak spectral dependence within this region. In contrast, clear-sky spectra show stronger wavelength-dependent variation, characterized by a more pronounced decrease toward longer wavelengths. More specifically, under clear-sky conditions the normalized zenith radiance generally peaks at 0.500 μm, while under cloudy conditions the peak tends to shift toward longer visible wavelengths, 0.675 μm. This systematic shift is consistently observed across the diverse environments represented by the eight SKYNET sites, including maritime, continental, tropical, and polar locations. The consistency of this behavior suggests that the observed spectral differences are governed primarily by fundamental atmospheric scattering processes rather than by site-specific characteristics.

The physical basis for this behavior can be explained by the dominant scattering mechanisms in clear and cloudy atmospheres. Under clear-sky conditions, zenith radiance is mainly controlled by molecular (Rayleigh) scattering and aerosol scattering. Rayleigh scattering exhibits a strong inverse dependence on wavelength (approximately proportional to λ^{-4}), resulting in enhanced scattering at shorter wavelengths in the blue portion of the spectrum. Aerosol scattering also exhibits wavelength dependence, though typically weaker than Rayleigh scattering. In the near-ultraviolet to blue spectral region, aerosol scattering can be typically several times smaller than Rayleigh scattering under low-to-moderate aerosol loading, although its relative contribution increases under polluted or dust-influenced conditions. As a result, clear-sky zenith radiance spectra tend to show relatively higher normalized radiance at shorter visible wavelengths and a gradual decrease toward longer wavelengths. In

https://doi.org/10.5194/egusphere-2026-2943
Preprint. Discussion started: 23 June 2026

contrast, under cloudy conditions the scattering of solar radiation is dominated by cloud droplets. The typical size of cloud droplets (on the order of several micrometers) is significantly larger than the wavelengths of visible light. Under these circumstances, scattering is primarily governed by Mie scattering, which exhibits much weaker wavelength dependence across the visible spectrum. Consequently, the scattered radiation becomes spectrally more uniform, producing flatter normalized radiance spectra compared with clear-sky conditions. Because shorter wavelengths are relatively less enhanced under this regime, the normalized spectral maximum tends to shift toward longer wavelengths in the visible region. These characteristics are consistent with theoretical descriptions of cloud scattering behavior (Bohren and Huffman, 2007; Hansen and Travis, 1974). Although the overall spectral behavior is consistent among the sites, minor variations in spectral shape are observed. These differences likely reflect variations in aerosol loading, aerosol type, solar geometry, and surface reflectance conditions. For example, sites influenced by maritime air masses or high aerosol concentrations may exhibit slightly modified spectral gradients due to changes in aerosol optical properties. Nevertheless, the fundamental contrast between clear- and cloudy-sky spectra remains evident across all environments.

4.1.2 Spectral Slopes

To better understand the spectral depenence of zenith radiances on wavelenths during clear- and cloudy-sky conditions, we analyzed the spectral slope values for all possible wavelength pairs, as given by Eq. (1). Figure 2 presents box-and-whisker distributions of slope values calculated from zenith radiance pairs for cloudy and confidently clear sky conditions at the Chiba site. Although results from other sites are not shown here for brevity, they exhibit slope patterns similar to those observed for Chiba. For shorter first wavelengths (λ_1 = 0.34–0.38 µm), the slope values are predominantly positive and relatively large. This behavior reflects the strong wavelength dependence of molecular (Rayleigh) scattering and aerosol scattering in the ultraviolet and blue spectral regions. Although some separation between cloudy and clear conditions is evident, the distributions partially overlap at these shorter wavelength regions. As the first wavelength shifts toward the visible and near-infrared region, the slope magnitude decreases and, for several wavelength combinations, become negative. The most distinct contrast between clear- and cloudy-sky conditions is observed for wavelength pairs with λ_1 between 0.400 and 0.675 µm. In particular, the wavelength pairs 0.400 and 0.675 µm, 0.500 and 0.675 µm, and 0.400 and 0.870 µm show clear separation between the two sky conditions, with predominantly negative slope values under clear skies and positive values under cloudy skies. Other wavelength pairs, such as 0.500 and 0.87 µm and 0.675 and 0.870 µm, also indicate differences in slope values between clear- and cloudy-sky conditions; however, the boundary values separating the two conditions tend to have the same sign, making threshold-based discrimination less straightforward. At longer wavelength (λ_1 = 0.87 µm), the absolute slope magnitude increases again, but the separation between cloudy and clear conditions becomes less consistent compared with above-mentioned wavelength pairs.

https://doi.org/10.5194/egusphere-2026-2943
Preprint. Discussion started: 23 June 2026

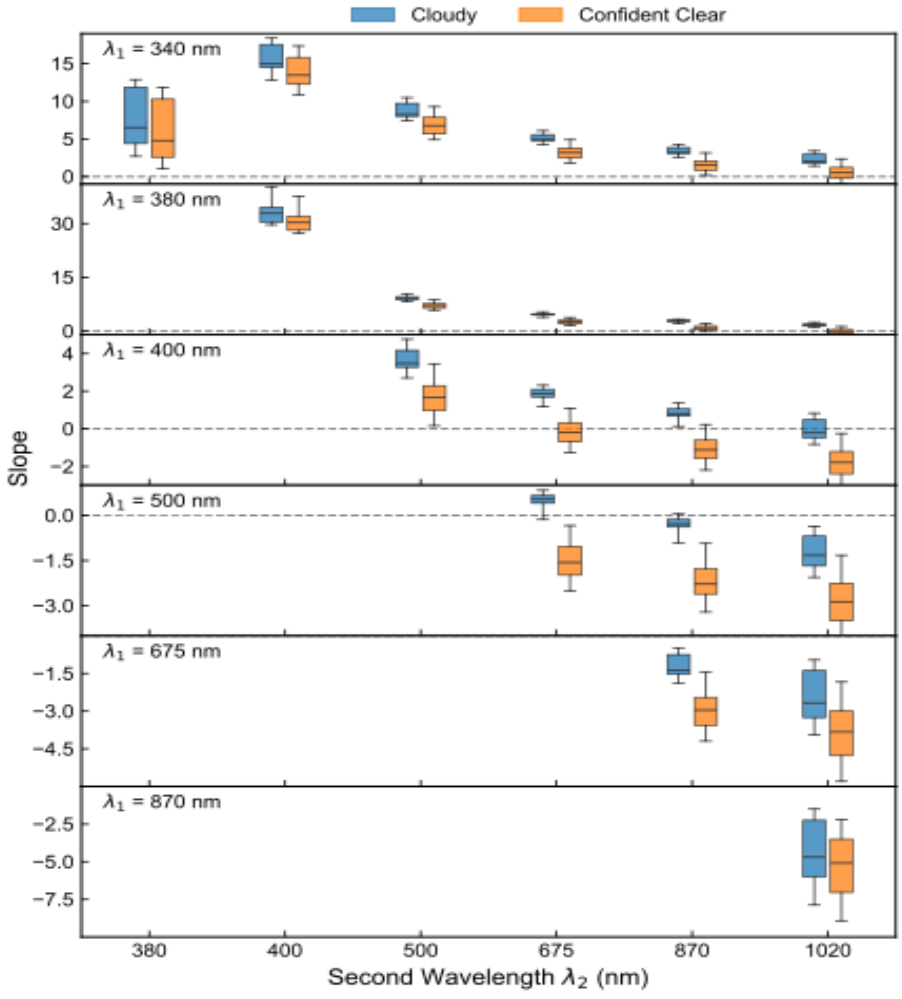

285 **Figure 2** . Box-and-whisker distributions of spectral slope values calculated from zenith radiance pairs for cloudy and confidently clear sky conditions for Chiba. Each row corresponds to a fixed first wavelength (λ_1), while the x-axis represents the second wavelength (λ_2). In the figure, the boxes represent the 25th and 75th percentiles, and the whiskers represent the 5th and 95th percentiles.

290

4.1.2.1 Dependence of Spectral Slope Values of Key Wavelength Pairs on Solar Geometery, Aerosol, and Cloud Conditions

As the three wavelength pairs—0.400 and 0.675 μm, 0.500 and 0.675 μm, and 0.400 and 0.870 μm—show predominant negative and positive slope values for clear- and cloudy-sky conditions, respectively, a more detailed analysis was performed
295 to understand their dependencies on solar position and aerosol and cloud optical properties. Specifically, we analyzed the dependence of the spectral slope on solar zenith angle (SZA), AOT, and AE under clear sky conditions identified using the reference MODIS cloud mask data. Similarly, for cloudy-sky conditions, we investigated the relationships between the spectral slope and SZA, COT, and CER. These analyses are shown in Figures 3 and 4.

300

https://doi.org/10.5194/egusphere-2026-2943
Preprint. Discussion started: 23 June 2026

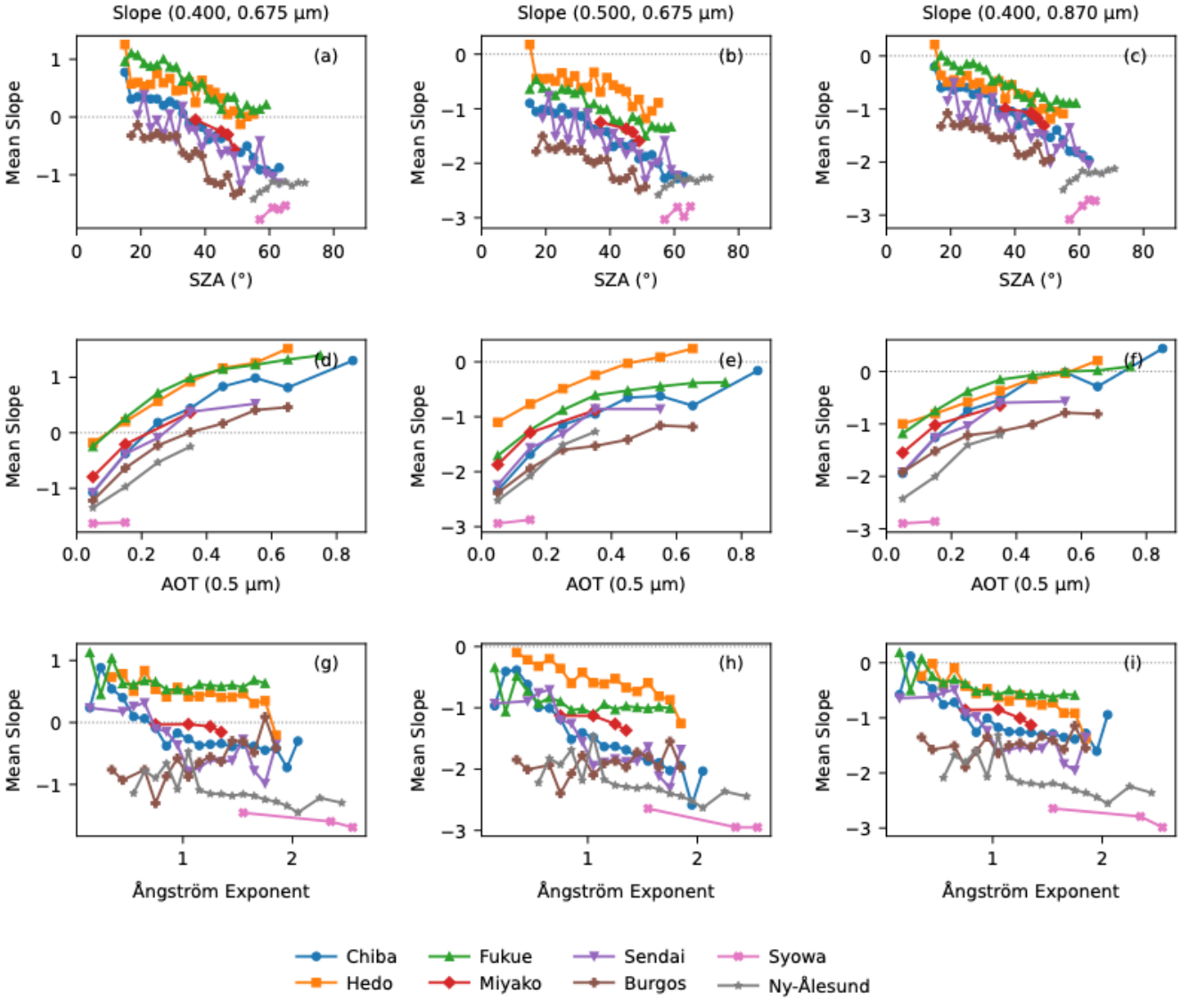

Figure 3. Dependence of mean spectral slope values on solar zenith angle, aerosol optical thickness, and Ångström exponent under clear-sky conditions identified using the reference MODIS cloud mask data. Mean values were calculated at each site using bin intervals of 2° for SZA, 0.1 for AOT, and 0.1 for the Ångström exponent.

https://doi.org/10.5194/egusphere-2026-2943
Preprint. Discussion started: 23 June 2026

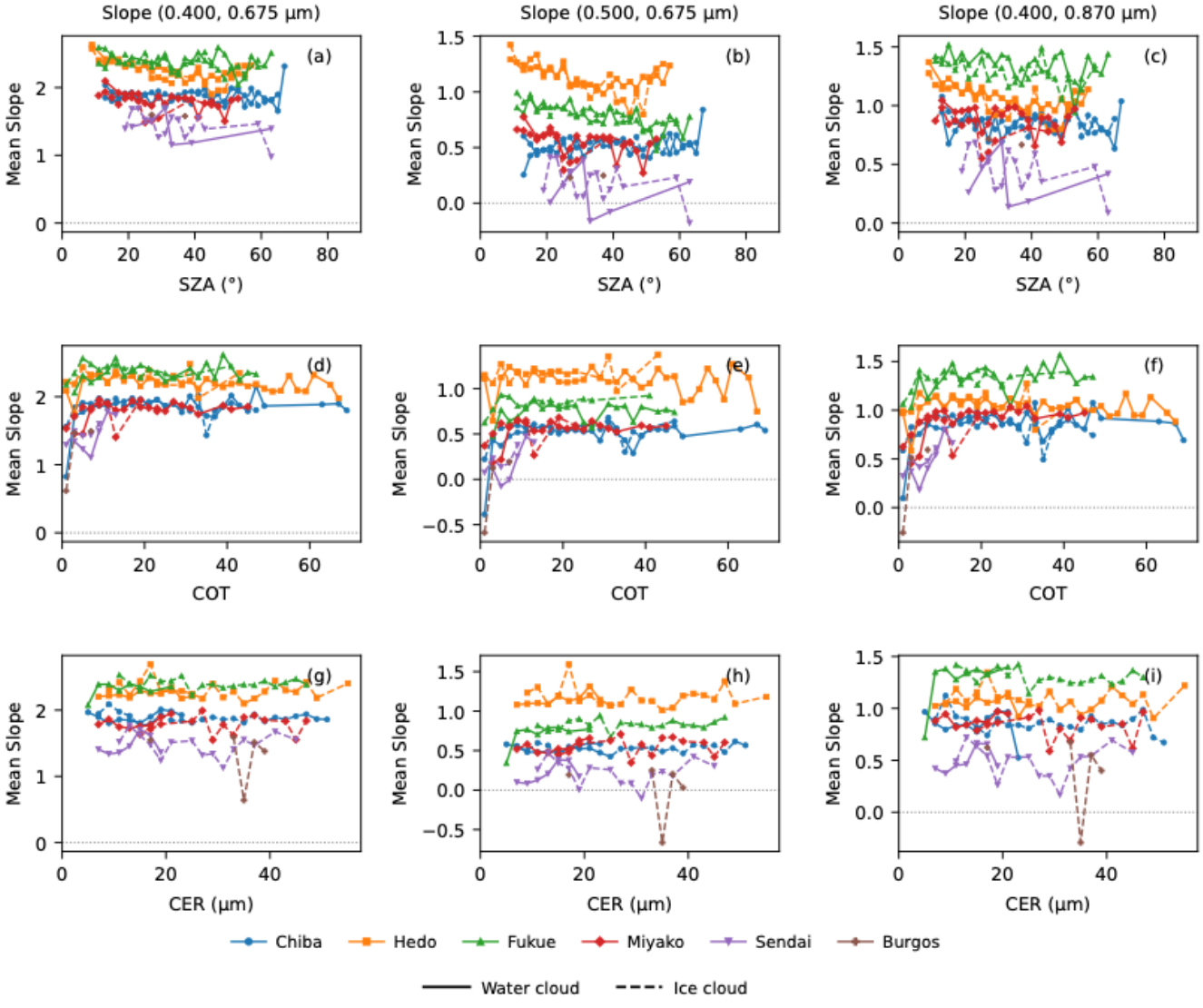

Figure 4. Dependence of mean spectral slope values on solar zenith angle, cloud optical thickness, and cloud effective radius under cloudy-sky conditions identified using the reference MODIS cloud mask data. Mean values were calculated at each site using bin intervals of 2° for SZA, 2 for COT, and 2 μm for CER.

Under clear-sky conditions, the mean slope generally decreases with increasing SZA. This behavior indicates that the spectral contrast of zenith radiance becomes stronger as the atmospheric optical path length increases. At larger SZA, enhanced Rayleigh and aerosol scattering along the longer slant path modifies the shortwave spectral distribution, leading to more negative slope values at most sites. This tendency is especially evident at mid- and low-latitude sites, whereas polar sites show weaker or somewhat different behavior, likely due to differences in aerosol loading, surface reflectance, and illumination geometry. The dependence on AOT differs from the SZA dependence. For all wavelenght pairs, one can note the increase of slope value with the increase of AOT. Particularly, the 0.500 and 0.675 μm pair remains predominantly negative even as AOT increases, although the slope becomes less negative under enhanced aerosol loading. This result indicates that the 0.500 and 0.675 μm pair retains a clear-sky signature over a wide range of aerosol conditions. Only under very high aerosol loading, such as at the maritime Hedo site, the slope values occasionally approach or exceed zero, possibly due to hygroscopic aerosol growth

https://doi.org/10.5194/egusphere-2026-2943
Preprint. Discussion started: 23 June 2026

under high relative humidity. The relationship between spectral slope and Ångström exponent is weaker and more site-dependent than the relationship with AOT. In some cases, the slope becomes slightly more negative with increasing Ångström exponent, but the pattern is not consistently monotonic across sites. This suggests that aerosol amount exerts a stronger first-order control on the slope magnitude than aerosol size information alone. The observed site-to-site variability may be related to differences in aerosol type, surface albedo, humidity-driven aerosol growth, and the limited sampling range of Ångström exponent at some sites.

Under cloudy conditions, the spectral slopes are predominantly positive for all examined wavelength combinations, clearly contrasting with the mostly negative slopes observed under clear skies. Among the tested pairs, the 0.400 and 0.675 μm pair generally shows the largest positive slope values, indicating strong sensitivity to cloudy-sky conditions. The 0.500 and 0.675 μm pair also shows positive values under clouds, although the magnitude is generally smaller and may occasionally approach zero. This contrast is physically meaningful as cloud scattering modifies the spectral distribution of zenith radiance in a way that reverses the sign of the slope relative to clear-sky conditions. The dependence of cloudy-sky slope on SZA is weaker than that observed under clear-sky conditions. Although some site-to-site variability is present, the slope generally remains positive across most SZA ranges. This indicates that cloud scattering dominates the spectral behavior of zenith radiance, reducing the relative influence of solar geometry compared with clear-sky cases. The slope also varies with COT, but the relationship is generally nonlinear. At low COT, the slope may change rapidly, indicating strong sensitivity to the transition from optically thin to moderately thick clouds. As COT increases, the slope tends to become more stable, suggesting that the zenith radiance spectrum approaches a saturated cloudy-sky regime. This is consistent with the expectation that, for optically thick clouds, additional increases in cloud optical thickness have a progressively smaller effect on radiance-based spectral signatures. The dependence on CER is weaker and more variable than the dependence on COT. For many sites, especially for water clouds, the mean slope remains relatively stable across the CER range. Ice cloud cases show larger variability, likely because ice cloud retrievals are more heterogeneous and are affected by particle habit, vertical structure, and possible mixed-phase contamination. Overall, the results demonstrate that the spectral slope is governed by different dominant physical factors under clear- and cloudy-sky conditions. Under clear skies, the slope is mainly influenced by solar geometry and aerosol optical loading, while under cloudy skies, it is primarily controlled by cloud scattering and COT.

4.1.2.2 Possibility of Clear- and Cloudy-Sky Discrimination

To identify wavelength-pair slope indices that are practically useful for discriminating between clear- and cloudy-sky conditions, we examined the classification performance of three wavelength pairs: 0.400 and 0.675 μm, 0.500 and 0.675 μm, and 0.400 and 0.87 μm. In this analysis, the sign of the spectral slope was used as a first-order indicator of sky condition: negative slope values were interpreted as clear-sky conditions, whereas positive slope values were interpreted as cloudy-sky conditions. The validity of this assumption was evaluated by comparing the slope-based classifications with MODIS cloud-mask-based sky classifications. The resulting confusion matrices for each wavelength pair are shown in Figures 5–7.

For the 0.400 and 0.675 μm wavelength pair (Figure 5), positive slope values successfully identify cloudy conditions at all sites, with cloudy-sky detection rates generally exceeding 95%. Particularly high cloudy-sky detection rates, approximately 95–100%, are obtained at Chiba, Hedo, Sendai, Syowa, Ny-Ålesund, and Burgos. However, this wavelength pair exhibits much larger site-to-site variability in clear-sky detection. Although Syowa and Ny-Ålesund show clear-sky detection rates above 90%, several mid- and low-latitude sites show frequent misclassification of MODIS-clear cases as cloudy. For example, the clear-sky detection rates are only 32.3% at Fukue, 27.9% at Hedo, and 58.2% at Chiba. This indicates that the 0.400 and 0.675 μm slope is highly sensitive to cloudy conditions but is less robust for identifying clear-sky conditions across different atmospheric environments.

For the 0.500 and 0.675 μm wavelength pair (Figure 6), clear-sky detection improves substantially. Clear-sky detection rates exceed 97% at Chiba, Fukue, Miyako, Sendai, Syowa, Ny-Ålesund, and Burgos, while Hedo shows a somewhat lower but still high value of 86.4%. Cloudy-sky detection is also high at several sites, exceeding 93% at Chiba, Fukue, Hedo, Miyako, and Ny-Ålesund. However, the cloudy-sky detection rate decreases at Sendai, Syowa, and Burgos, where values fall within approximately 75–86%. Thus, the 0.500 and 0.675 μm pair is particularly effective for detecting clear-sky conditions, although its sensitivity to cloudy conditions is somewhat more site-dependent.

The 0.400 and 0.870 μm wavelength pair (Figure 7) shows a more balanced performance. Clear-sky detection rates are generally above 88%, reaching 100% at Miyako and Burgos, while cloudy-sky detection remains high at several sites,

https://doi.org/10.5194/egusphere-2026-2943
Preprint. Discussion started: 23 June 2026

especially Chiba, Fukue, Hedo, Miyako, and Ny-Ålesund. Compared with the other two wavelength pairs, the 0.400 and 0.870 μm pair provides a more stable compromise between clear- and cloudy-sky detection, suggesting that it is less affected by site-specific atmospheric conditions.

To quantify the relative performance of the three wavelength-pair slope indices, we calculated three classification metrics: clear recall, cloudy recall, and balanced accuracy. These are defined as follows:

$$\text{Clear Recall} = \frac{\text{TN}}{\text{TN+FP}}, \quad (3)$$

$$\text{Cloudy Recall} = \frac{\text{TP}}{\text{TP+FN}}, \quad (4)$$

$$\text{Balanced Accuracy} = \frac{1}{2}(\text{Clear Recall+Cloudy Recall}), \quad (5)$$

where TN, FP, TP, and FN denote true negative, false positive, true positive, and false negative, respectively. In this study, clear-sky conditions are treated as the negative class and cloudy-sky conditions as the positive class. Therefore, clear recall represents the fraction of MODIS-clear cases correctly identified as clear by the slope method, whereas cloudy recall represents the fraction of MODIS-cloudy cases correctly identified as cloudy. The site-averaged values of these metrics are summarized in Table 2.

Table 2. Performance comparison of three wavelength-pair slope indices for clear/cloudy discrimination using MODIS cloud mask as the reference

Wavelength pair	Mean clear recall	Mean cloudy recall	Balanced accuracy	Site-to-site Standard Deviation
0.400 and 0.675 μm	64.6%	98.2%	81.4%	11.7%
0.500 and 0.675 μm	97.2%	90.0%	93.6%	4.2%
0.400 and 0.870 μm	95.8%	92.6%	94.2%	3.1%

Overall, these results indicate that the 0.400 and 0.675 μm wavelength pair is highly sensitive to cloudy-sky conditions but has relatively poor and site-dependent sensitivity to clear-sky conditions. In contrast, the 0.500 and 0.675 μm and 0.400 and 0.870 μm wavelength pairs provide substantially more balanced discrimination between clear and cloudy skies. Among them, the 0.400 and 0.870 μm pair yields the highest balanced accuracy and the smallest site-to-site variability, whereas the 0.500 and 0.675 μm pair provides the highest mean clear recall. These results suggest that both the 0.400 and 0.870 μm and 0.500 and 0.675 μm wavelength pairs are practically useful for first-order clear- and cloudy-sky discrimination without requiring auxiliary data or complex statistical procedures.

However, it should be noted that a zero-slope threshold is not necessarily the mathematically optimal decision boundary for every site. Its advantage is instead practical and physical: the sign change of the slope reflects a change in the spectral behavior of zenith radiance between clear- and cloudy-sky conditions. In the binary classification described above, every observation is forced into either a clear-sky or cloudy-sky category. In practice, however, slope values close to zero are inherently uncertain because they indicate weak spectral contrast between the selected wavelengths. These cases may correspond to optically thin clouds, partly cloudy scenes, aerosol-loaded clear skies, low solar-elevation conditions, or mixed satellite-pixel conditions. Therefore, for operational or practical applications, it is more reasonable to introduce a tolerance range around zero, $\pm\varepsilon$, and classify observations within this range as undetermined. This approach preserves the physical interpretability of the slope sign while reducing uncertain classifications near the decision boundary.

A practical slope-based classification scheme can therefore be formulated as follows. Let $S_{0.5-0.675}$ and $S_{0.4-0.87}$ denote the spectral slopes for the 0.500 and 0.675 μm and 0.400 and 0.870 μm wavelength pairs, respectively. Then,

$$\text{Clear sky: } S_{0.5-0.675} < -\varepsilon \quad \text{and/or } S_{0.4-0.87} < -\varepsilon, \quad (6)$$

$$\text{Cloudy sky: } S_{0.5-0.675} > +\varepsilon \text{ and/or } S_{0.4-0.87} > +\varepsilon, \quad (7)$$

$$\text{Undetermined: } -\varepsilon \le S_{0.5-0.675} \le +\varepsilon \text{ or } -\varepsilon \le S_{0.4-0.87} \le +\varepsilon, \quad (8)$$

https://doi.org/10.5194/egusphere-2026-2943
Preprint. Discussion started: 23 June 2026

or when the two slope indices provide conflicting indications. For strict sky-state detection, the logical operator "and" may be used, requiring both slope indices to satisfy the same criterion. Conversely, the "or" operator provides a more inclusive classification, in which either slope index satisfying the criterion is sufficient for classification.

Here, ε acts as a tolerance parameter that defines the width of the uncertain region around the zero-slope boundary. A smaller ε produces a more inclusive classification but may retain more ambiguous cases, whereas a larger ε produces a stricter classification with fewer but more reliable clear- and cloudy-sky samples.

For a conservative and robust classification, the two wavelength pairs can be combined using logical rules. For example, a strict clear-sky classification may require both $S_{0.5-0.675}$ and $S_{0.4-0.87}$ to be smaller than $-\varepsilon$, whereas a strict cloudy-sky classification may require both slopes to be larger than $+\varepsilon$. Cases in which only one slope satisfies the criterion, or in which the two slopes provide inconsistent indications, can be assigned to the undetermined category. Such a combined approach takes advantage of the high clear-sky sensitivity of the 0.500 and 0.675 µm pair and the balanced performance of the 0.400 and 0.870 µm pair, while reducing the risk of overconfident classification near the threshold.

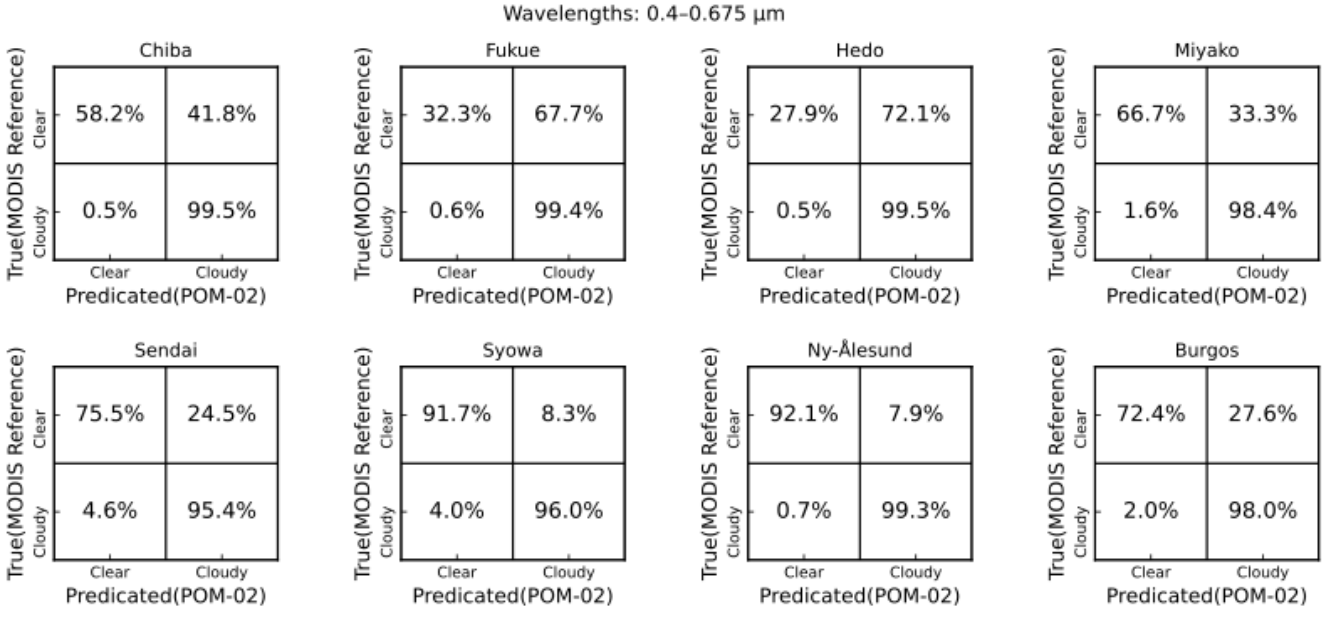

Figure 5. Confusion matrices for clear- and cloudy-sky discrimination using the sign of the spectral slope between 0.400 and 0.675 µm. Negative and positive slope values are classified as clear and cloudy conditions, respectively. MODIS cloud-mask classifications are used as the reference, while POM-02 slope-based classifications are treated as predictions. Each matrix is normalized by the MODIS reference class, so that each row sums to 100%.

https://doi.org/10.5194/egusphere-2026-2943
Preprint. Discussion started: 23 June 2026

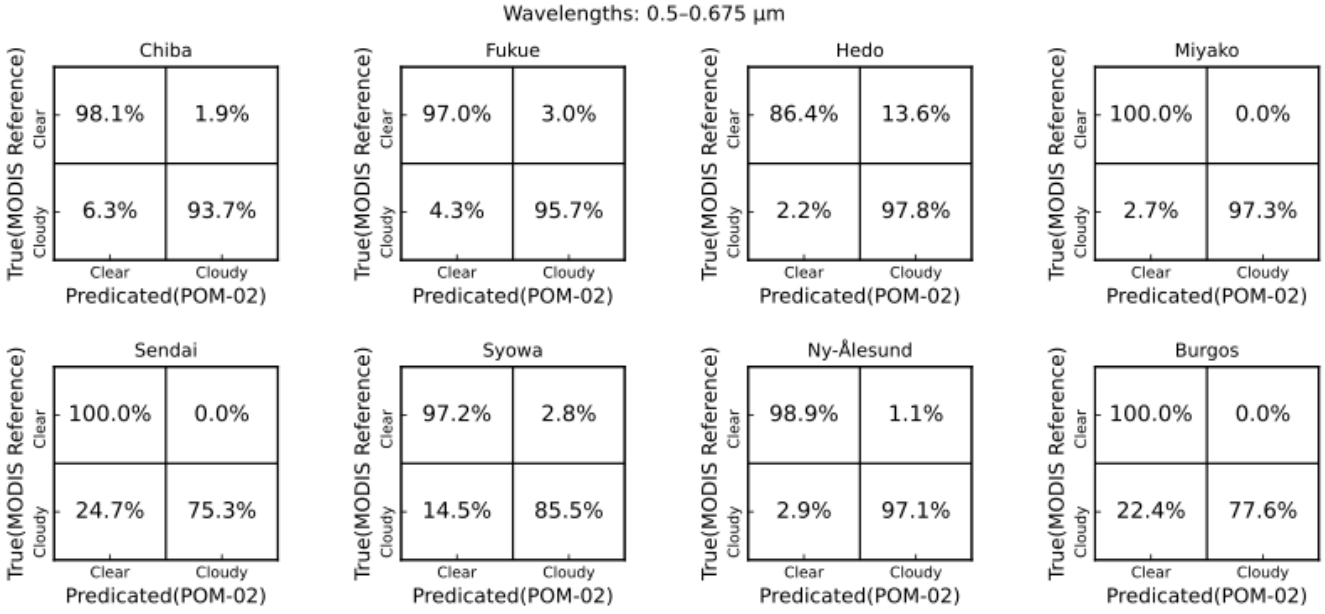

Figure 6. Same as Fig. 3, but for the spectral slope between 0.500 and 0.675 µm.

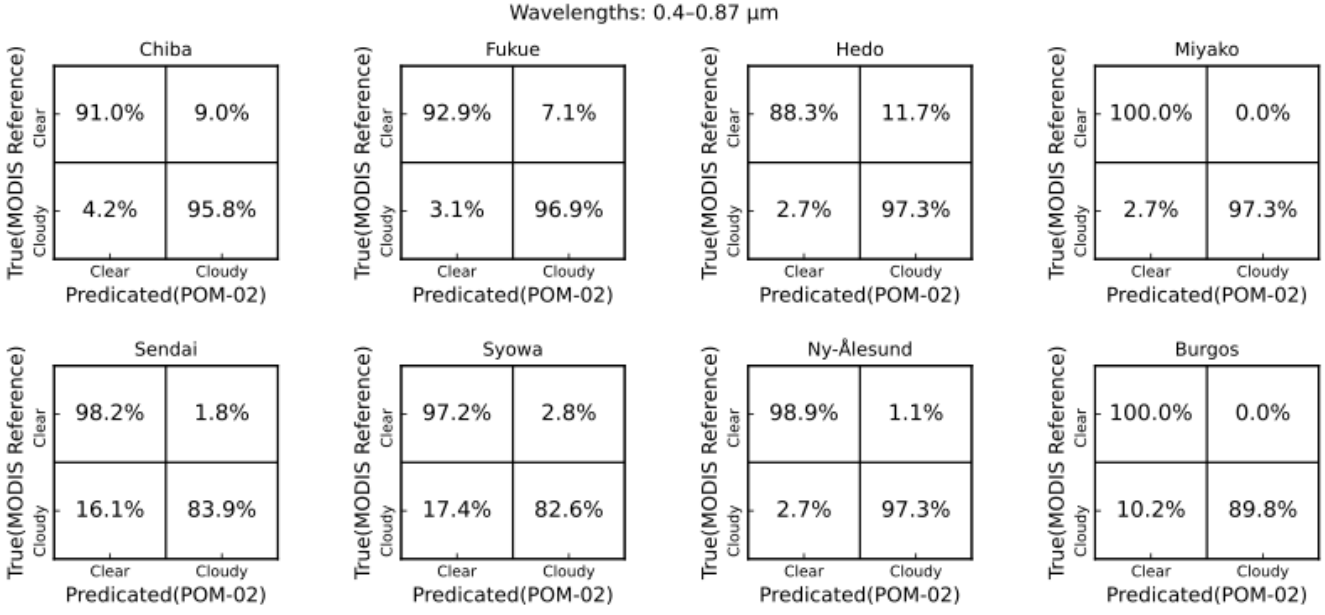

Figure 7. Same as Fig. 3, but for the spectral slope between 0.400 and 0.870 µm.

https://doi.org/10.5194/egusphere-2026-2943
Preprint. Discussion started: 23 June 2026

4.2 Validation of the Spectral Slope Criterion Using Direct Normal Irradiance

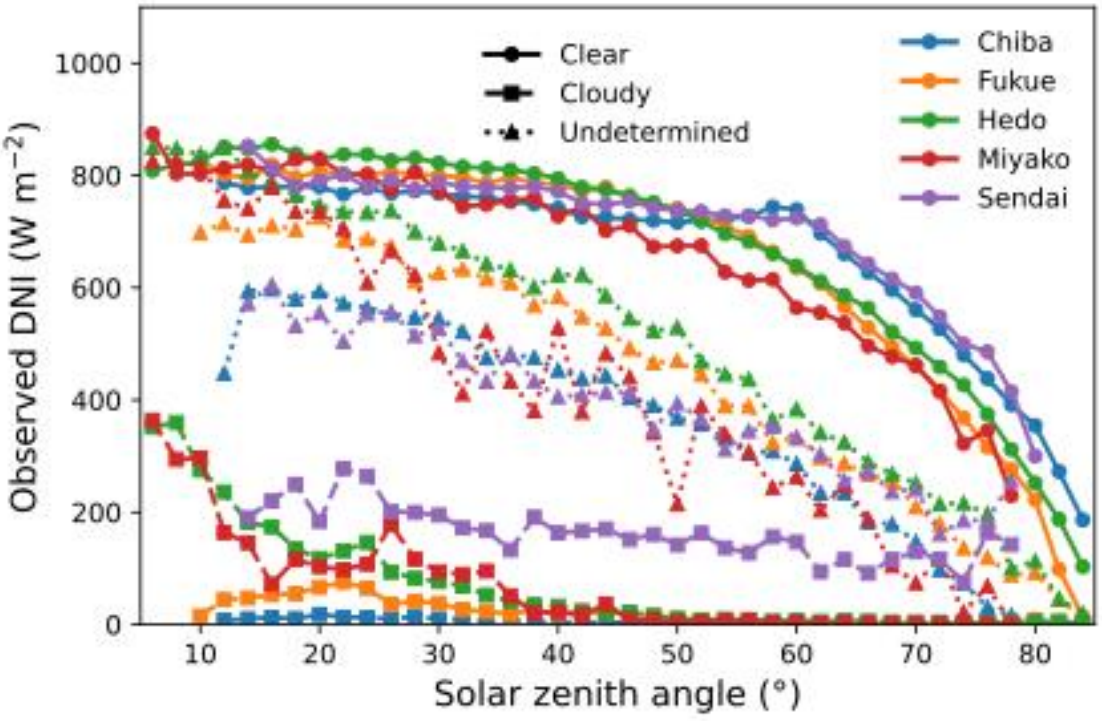

Figure 8. Relationship between median values of observed direct normal irradiance (DNI) within a 2° solar zenith angle (SZA) bin and SZA for clear, cloudy, and undetermined conditions predicted using wavelength pairs of 0.500 and 0.675 μm and 0.400 and 0.875 μm with ε = 0.05 at (a) Chiba, (b) Hedo, (c) Fukue, (d) Miyako, and (e)Sendai.

To evaluate the applicability of the combined spectral-slope criteria for discriminating clear, cloudy, and ambiguous sky conditions, direct normal irradiance (DNI) measurements obtained from pyrheliometers were analyzed together with sky radiometer observations. DNI provides an independent physical indicator of sky condition because it represents the direct solar beam reaching the surface and is therefore highly sensitive to cloud attenuation. Under clear-sky conditions, DNI is expected to remain relatively high and to decrease smoothly with increasing solar zenith angle (SZA) mainly because of increasing atmospheric air mass. Under cloudy conditions, DNI is strongly reduced because clouds attenuate or block the direct solar beam.

Figure 8 shows the relationship between median observed DNI and SZA for five observation sites: Chiba, Fukue, Hedo, Miyako, and Sendai. The median DNI values were calculated within 2° SZA bins. Sky conditions were classified using two spectral-slope features derived from the 0.500 and 0.675 μm and 0.400 and 0.875 μm wavelength pairs. A conservative threshold of ε = 0.05 was applied: clear conditions were assigned when both slopes were smaller than −ε, cloudy conditions when both slopes were larger than +ε, and all remaining cases were classified as undetermined.

Across all five sites, the clear-sky class exhibits high median DNI values over low to moderate SZAs, followed by a gradual decrease at larger SZAs. This behavior is physically consistent with direct-beam transmission under cloud-free conditions, where the dominant SZA dependence is controlled by geometric air-mass effects. The clear-sky curves are especially coherent among the sites, although site-to-site differences are visible because of differences in aerosol loading, water vapor, surface environment, and sampling conditions.

https://doi.org/10.5194/egusphere-2026-2943
Preprint. Discussion started: 23 June 2026

In contrast, the cloudy class is characterized by substantially lower median DNI values over most SZA ranges. For several sites, cloudy-sky DNI values rapidly decrease to near-zero levels, indicating strong attenuation of the direct solar beam by clouds. This confirms that the combined positive-slope criterion successfully identifies conditions in which direct solar radiation is strongly suppressed.

The undetermined class occupies an intermediate regime between the clear and cloudy classes. Its median DNI values are generally lower than those of the clear class but higher and more variable than those of the cloudy class. This behavior is physically reasonable because the undetermined category includes cases where the two slope criteria do not provide a consistent classification, such as thin clouds, broken clouds, cloud-edge conditions, aerosol-influenced cases, or transitional sky conditions. Therefore, the undetermined group should not be interpreted as classification failure, but rather as a conservative buffer zone that prevents uncertain cases from being forced into either the clear or cloudy category.

Overall, the clear, cloudy, and undetermined DNI regimes are well separated. The high and smoothly varying DNI values for the clear class, the strongly reduced DNI values for the cloudy class, and the intermediate behavior of the undetermined class demonstrate that the combined use of the 0.500 and 0.675 μm and 0.400 and 0.875 μm spectral-slope criteria provides a physically consistent and conservative method for sky-condition discrimination. The results may also indicate that introducing an undetermined category is useful for improving the robustness of the method, especially under mixed or transitional atmospheric conditions.

4.3 Comparison with Results from Existing Standard Clear- and Cloudy-Sky Detection Procedure

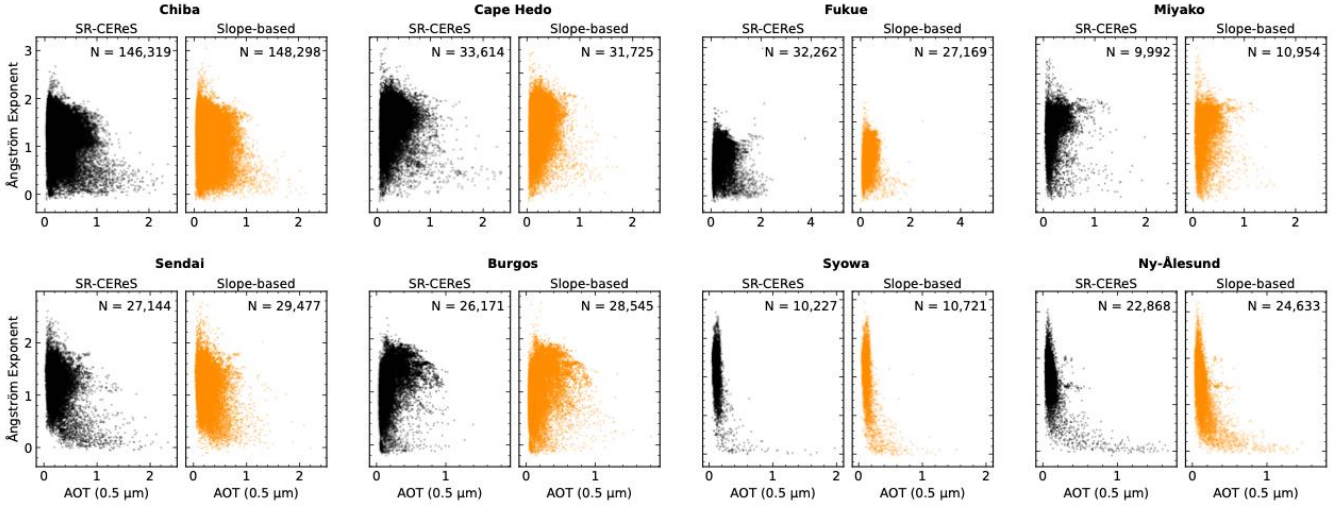

Figure 9. Scatter plots of Ångström exponent (AE) versus aerosol optical thickness at 0.5 μm (AOT) for eight SKYNET sites after cloud screening using two algorithms: the standard SR-CEReS package (left panels) and the slope-based method derived from the spectral slopes of zenith radiance between 0.5 and 0.675 μm and 0.400 and 0.870 μm with ε value of 0.05 (right panels). Numbers indicate the total observations retained by each method.

To evaluate the performance of the slope-based cloud screening approach, the relationship between AOT (0.5 μm) and AE derived from Eq. (2) was compared with results obtained using the standard SR-CEReS package. Figure 5 presents AE–AOT scatter plots for eight SKYNET sites representing diverse atmospheric environments, as summarized in Table 1. Here, we used the criteria of $S_{0.5-0.675} < -\varepsilon$ and $S_{0.4-0.87} < -\varepsilon$ with ε value of 0.05.

Overall, the AE–AOT distributions obtained using the slope-based method closely resemble those derived from the SR-CEReS outputs across all sites. In particular, the slope-based screening method reproduces the distinct aerosol regimes characteristic

https://doi.org/10.5194/egusphere-2026-2943
Preprint. Discussion started: 23 June 2026

of each observation site. For example, relatively large AE values and broader AOT variability observed at the sites within Japan suggest the influence of both anthropogenic fine-mode aerosols and particles transported from surrounding oceanic and continental regions, including desert areas, via long-range transport. In contrast, the tropical continental site, Burgos, shows relatively high AE values associated with biomass burning and anthropogenic aerosols commonly observed in Southeast Asia. The polar sites—Syowa and Ny-Ålesund—exhibit very low AOT values and relatively narrow AE distributions, reflecting the extremely clean atmospheric conditions typical of polar regions. The ability of the slope-based method to reproduce these site-dependent aerosol characteristics indicates that the proposed screening approach does not introduce significant biases in the cloud-screened aerosol optical properties. Because the clear-sky detection criterion given in Eq. (6) is flexible, the screening can be made either stricter or more relaxed through an appropriate choice of logical operator and/or ε, depending on the application requirements. Nonetheless, the good agreement with the SR-CEReS results demonstrates that the proposed slope-based approach provides a practical and physically consistent method for cloud screening in SKYNET aerosol retrievals.

5 Conclusions

This study investigated the spectral characteristics of zenith sky radiance measurements from SKYNET sky radiometers under clear- and cloudy-sky conditions identified using quality-controlloed MODIS cloud mask products. The study also examined the potential for discriminating between these sky conditions using spectral information. By analyzing normalized spectral radiance behavior across wavelengths with minimal absorption by atmospheric gases at multiple SKYNET sites representing diverse atmospheric environments, systematic and physically consistent differences between clear- and cloudy-sky conditions were identified.

The analysis revealed that cloudy skies exhibit relatively flatter spectral behavior in the visible region, whereas clear skies show stronger wavelength dependence consistent with Rayleigh and aerosol scattering processes. Among the wavelength combinations examined, 0.400 and 0.675 µm wavelength pair showed high sensitivity to cloudy-sky conditions and enabled more accurate identification of cloudy cases; however, it performed poorly in detecting clear-sky conditions. In contrast, the 0.500 an 0.675 µm and 0.400 and 0.870 µm pairs showed relatively higher sensitivity to clear-sky conditions and provided more balanced discrimination between clear and cloudy skies. Specifically, the spectral slope, defined as the ratio of the natural logarithm of the zenith radiance ratio at the shorter and longer wavelengths to the natural logarithm of the corresponding wavelength ratio, showed predominantly negative values under clear skies and positive under cloudy skies. Furthermore, the spectral slope was controlled mainly by solar geometry and aerosol optical loading under clear skies, but under cloudy-skies, the dependence behaviours on solar geometry and cloud optical properties were weaker than those for clear-sky conditions. Those behavior can arise because clear-sky radiance retains stronger wavelength dependence, whereas cloud droplets scatter radiation more uniformly across the visible spectrum.

These observation-based results were systematically integrated to develop a flexible, easy-to-use, and computationally efficient sky-state detection criterion that allows an uncertainty margin around the boundary between clear- and cloudy-sky regimes. The robustness of the proposed criterion was further validated using collocated DNI measurements across different atmospehric regimes. The cases identified as clear-skies corresponded to high DNI values that varied smoothly with solar zenith angle, characteristic of clear-sky radiative transfer. In contrast, cases identified as cloudy skies were associated with substantially reduced DNI values, reflecting strong attenuation of the direct solar beam by clouds. Further, DNI values corresponding to undetermined cases existed between those for clear and cloudy sky conditions. This clear separation in DNI distributions across geographically and climatologically distinct sites confirms the physical consistency of the proposed slope-based classification approach for detecting clear- and cloudy-sky conditions easily and smoothly.

To further evaluate the performance of the slope-based screening approach, cloud-screend aerosol optical properties using our developed criterion were compared with those derived from the standard SR-CEReS package. The AE–AOT relationships obtained from both approaches showed strong agreement across multiple observation sites representing urban, maritime,

https://doi.org/10.5194/egusphere-2026-2943
Preprint. Discussion started: 23 June 2026

tropical continental, and polar environments. In particular, the slope-based method successfully reproduced the characteristic aerosol regimes observed at each site without introducing noticeable biases in the retrieved aerosol optical properties.
Overall, the results demonstrate that the spectral sky zenith radainces observed by sky radiometer provide a very powerful informaiton to detect sky states reasonablly without substantial computational burden or auxiliary data from other sources. Because the method relies on spectral shape rather than absolute radiance magnitude, it is relatively insensitive to calibration uncertainties and can be applied across diverse atmospheric environments. Therefore, spectral slope diagnostics of zenith radiances can serve as a reliable and computationally efficient complementary tool for cloud detection in SKYNET observations and other ground-based radiometric networks measuring zenith radiance.

Author Contributions: Conceptualization, P. K. and H. I.; methodology, P. K.; software, P. K.; formal analysis, P. K.; investigation, P. K.; resources, H.I., H. K., I. M., T. H., H. I, and T. T. ; writing—original draft preparation, P. K.; writing—review and editing, P. K., T.H, I. M, Y. J, and Y. T.; funding acquisition, P. K. All authors have read and agreed to the published version of the manuscript.

Funding: This research was funded by JSPS KAKENHI Grant Number 24K07129 and collaborative research fund of Center for Environmental Remote Sensing (CEReS), Chiba University of Fiscal year 2025.

Data Availability Statement: MODIS data used in this study were obtained from the NASA Earthdata Search portal (https://search.earthdata.nasa.gov/). Aerosol optical thickness (AOT) data were downloaded from the SKYNET website (http://atmos3.cr.chiba-u.jp/skynet/). The spectral zenith sky radiance data used in this study are available from the respective site owners upon reasonable request. The Burgos SKYNET operation is supported in part by the GOSAT series project. Local support for Burgos is provided by the Energy Development Corporation (EDC, the Philippines). Similarly, the observation data from Showa Station in Antarctica and Ny-Ålesund in the Arctic were collected as part of the National Institute of Polar Research's monitoring observations.

Conflicts of Interest: Authors have no conflict of interest.

References

Ackerman, S. A., Strabala, K. I., Menzel, W. P., Frey, R. A., Moeller, C. C., and Gumley, L. E.: Discriminating clear sky from clouds with MODIS, Journal of Geophysical Research Atmospheres, 103, 32141–32157, https://doi.org/10.1029/1998JD200032, 1998.

Bagtasa, G., Cayetano, M. G., and Yuan, C. S.: Seasonal variation and chemical characterization of PM2.5 in northwestern Philippines, Atmos. Chem. Phys., 18, 4965–4980, https://doi.org/10.5194/acp-18-4965-2018, 2018.

Bi, J., Shi, J., Xie, Y., Liu, Y., Takamura, T., and Khatri, P.: Dust aerosol characteristics and shortwave radiative impact at a gobi desert of northwest China during the spring of 2012, Journal of the Meteorological Society of Japan, 92A, 33–56, https://doi.org/10.2151/jmsj.2014-A03, 2014.

Bohren, C. F. and Huffman, D. R.: Absorption and Scattering of Light by Small Particles, wiley, 1–530 pp., https://doi.org/10.1002/9783527618156, 2007.

Campanelli, M., Nakajima, T., Khatri, P., Takamura, T., Uchiyama, A., Estelles, V., Liberti, G. L., and Malvestuto, V.: Retrieval of characteristic parameters for water vapour transmittance in the development of ground-based sun-sky radiometric measurements of columnar water vapour, Atmos. Meas. Tech., 7, 1075–1087, https://doi.org/10.5194/amt-7-1075-2014, 2014.

Damiani, A., Irie, H., Takamura, T., Kudo, R., Khatri, P., Iwabuchi, H., Masuda, R., and Nagao, T.: An Intensive Campaign-Based Intercomparison of Cloud Optical Depth from Ground and Satellite Instruments under Overcast Conditions, Sola, 15, 198–204, https://doi.org/10.2151/sola.2019-036, 2019.

https://doi.org/10.5194/egusphere-2026-2943
Preprint. Discussion started: 23 June 2026

Dim, J. R., Takamura, T., Higurashi, A., Kathri, P., Kikuchi, N., and Nakajima, T. Y.: Validation of Two MODIS aerosols algorithms with SKYNET and prospects for future climate satellites such as the GCOM-C/SGLI, Advances in Meteorology, 2013, https://doi.org/10.1155/2013/508064, 2013.

Hansen, J. E. and Travis, L. D.: Light scattering in planetary atmospheres, Space Sci. Rev., 16, 527–610, 1974.

Hara, K., Osato, K., Yabuki, M., Osada, K., Hirasawa, N., Shiobara, M., and Yamanouchi, T.: Antarctic haze phenomena at Syowa Station, Antarctica: seasonal features and impacts on atmospheric chemistry, NPJ Clim. Atmos. Sci., 8, https://doi.org/10.1038/s41612-025-01176-9, 2025.

Hashimoto, M., Nakajima, T., Dubovik, O., Campanelli, M., Che, H., Khatri, P., Takamura, T., and Pandithurai, G.: Development of a new data-processing method for SKYNET sky radiometer observations, Atmos. Meas. Tech., 5, 2723–2737, https://doi.org/10.5194/amt-5-2723-2012, 2012.

Holben, B. N., Eck, T. F., Slutsker, I., Tanré, D., Buis, J. P., Setzer, A., Vermote, E., Reagan, J. A., Kaufman, Y. J., Nakajima, T., Lavenu, F., Jankowiak, I., and Smirnov, A.: AERONET—A Federated Instrument Network and Data Archive for Aerosol Characterization, Remote Sens. Environ., 66, 1–16, https://doi.org/10.1016/S0034-4257(98)00031-5, 1998.

IPCC: Climate Change 2021: The Physical Science Basis. Contribution of Working Group I to the Sixth Assessment Report of the Intergovernmental Panel on Climate Change, edited by: Masson-Delmotte, V., Zhai, P., Pirani, A., Connors, S. L., Péan, C., Berger, S., Caud, N., Chen, Y., Goldfarb, L., Gomis, M. I., Huang, M., Leitzell, K., Lonnoy, E., Matthews, J. B. R., Maycock, T. K., Waterfield, T., Yelekçi, O., Yu, R., and Zhou, B., Cambridge University Press, Cambridge, United Kingdom and New York, NY, USA, 2391 pp., https://doi.org/10.1017/9781009157896, 2023.

Irie, H., Mohammed Syedul Hoque, H., Damiani, A., Okamoto, H., Mashroor Fatmi, A., Khatri, P., Takamura, T., and Jarupongsakul, T.: Simultaneous observations by sky radiometer and MAX-DOAS for characterization of biomass burning plumes in central Thailand in January-April 2016, Atmos. Meas. Tech., 12, 599–606, https://doi.org/10.5194/amt-12-599-2019, 2019.

Khatri, P. and Takamura, T.: An algorithm to screen cloud-affected data for sky radiometer data analysis, Journal of the Meteorological Society of Japan, 87, 189–204, https://doi.org/10.2151/jmsj.87.189, 2009.

Khatri, P., Takamura, T., Shimizu, A., and Sugimoto, N.: Spectral dependency of aerosol light-absorption over the East China sea region, Scientific Online Letters on the Atmosphere, 6, 1–4, https://doi.org/10.2151/sola.2010-001, 2010.

Khatri, P., Takamura, T., Shimizu, A., and Sugimoto, N.: Observation of low single scattering albedo of aerosols in the downwind of the East Asian desert and urban areas during the inflow of dust aerosols, J. Geophys. Res., 119, 787–802, https://doi.org/10.1002/2013JD019961, 2014a.

Khatri, P., Takamura, T., Yamazaki, A., and Uchiyama, A.: Use of 315 nm channel data of the sky radiometer to estimate the columnar ozone concentration: A preliminary study, Journal of the Meteorological Society of Japan, 92A, 185–194, https://doi.org/10.2151/jmsj.2014-A12, 2014b.

Khatri, P., Hayasaka, T., Iwabuchi, H., Takamura, T., Irie, H., and Nakajima, T. Y.: Validation of MODIS and AHI observed water cloud properties using surface radiation data, Journal of the Meteorological Society of Japan, 96B, 151, https://doi.org/10.2151/jmsj.2018-036, 2018.

Khatri, P., Iwabuchi, H., Hayasaka, T., Irie, H., Takamura, T., Yamazaki, A., Damiani, A., Letu, H., and Kai, Q.: Retrieval of cloud properties from spectral zenith radiances observed by sky radiometers, Atmos. Meas. Tech., 12, 6037–6047, https://doi.org/10.5194/amt-12-6037-2019, 2019.

Khatri, P., Hayasaka, T., Irie, H., Letu, H., Nakajima, T. Y., Ishimoto, H., and Takamura, T.: Quality assessment of Second-generation Global Imager (SGLI)-observed cloud properties using SKYNET surface observation data, Atmos. Meas. Tech., 15, 1967–1982, https://doi.org/10.5194/amt-15-1967-2022, 2022.

Nakajima, T., Campanelli, M., Che, H., Estellés, V., Irie, H., Kim, S. W., Kim, J., Liu, D., Nishizawa, T., Pandithurai, G., Kumar Soni, V., Thana, B., Tugjsurn, N. U., Aoki, K., Go, S., Hashimoto, M., Higurashi, A., Kazadzis, S., Khatri, P., Kouremeti, N., Kudo, R., Marenco, F., Momoi, M., Ningombam, S. S., Ryder, C. L., Uchiyama, A., and Yamazaki, A.: An overview of and issues with sky radiometer technology and SKYNET, Atmos. Meas. Tech., 13, 4195–4218, https://doi.org/10.5194/amt-13-4195-2020, 2020.

Ningombam, S. S., Larson, E. J. L., Indira, G., Madhavan, B. L., and Khatri, P.: Aerosol classification by application of machine learning spectral clustering algorithm, Atmos. Pollut. Res., 15, https://doi.org/10.1016/j.apr.2023.102026, 2024.

Pasquier, J. T., David, R. O., Freitas, G., Gierens, R., Gramlich, Y., Haslett, S., Li, G., Schäfer, B., Siegel, K., Wieder, J., Adachi, K., Belosi, F., Carlsen, T., Decesari, S., Ebell, K., Gilardoni, S., Gysel-Beer, M., Henneberger, J., Inoue, J., Kanji,

https://doi.org/10.5194/egusphere-2026-2943
Preprint. Discussion started: 23 June 2026

Z. A., Koike, M., Kondo, Y., Krejci, R., Lohmann, U., Maturilli, M., Mazzolla, M., Modini, R., Mohr, C., Motos, G., Nenes, A., Nicosia, A., Ohata, S., Paglione, M., Park, S., Pileci, R. E., Ramelli, F., Rinaldi, M., Ritter, C., Sato, K., Storelvmo, T., Tobo, Y., Traversi, R., Viola, A., and Zieger, P.: The Ny-Ålesund Aerosol Cloud Experiment (NASCENT) Overview and First Results, Bull. Am. Meteorol. Soc., 103, E2533–E2558, https://doi.org/10.1175/BAMS-D-21-0034.1, 2022.

Platnick, S., Meyer, K., King, M. D., Wind, G., Amarasinge, N., Marchant, B., Arnold, G. T., Zhibo, Z., Hubanks, P. A., Holz, R. E., Yang, P., Ridgway, W. L., and Riedi, J.: The MODIS cloud optical and microphysical products: Collection 6 updates and examples from terra and aqua, IEEE Transactions on Geoscience and Remote Sensing, 55, 502–525, https://doi.org/10.1109/TGRS.2016.2610522, 2017.

Shiobara, M., Hayasaka, T., Nakajima, T., and Tanaka, M.: Aerosol Monitoring Using a Scanning Spectral Radiometer in Sendai, Japan, 1991.

Song, H. J., Sohn, B. J., Chun, H. W., Chun, Y., and Lee, S. S.: Improved cloud screening method for the analysis of sky radiometer measurements and application to asian dust detection, Journal of the Meteorological Society of Japan, 92A, 167–183, https://doi.org/10.2151/jmsj.2014-A11, 2014.

Nakajima, T. and King, M. D.: Determination of the Optical Thickness and Effective Particle Radius of Clouds from Reflected Solar Radiation Measurements. Part I: Theory, J. Atmos. Sci., 47, 1878–1893, https://doi.org/https://doi.org/10.1175/1520-0469(1990)047<1878:DOTOTA>2.0.CO;2, 1990.

Wang, Z., Liu, D., Wang, Z., Wang, Y., Khatri, P., Zhou, J., Takamura, T., and Shi, G.: Seasonal characteristics of aerosol optical properties at the SKYNET Hefei site (31.90°N, 117.17°E) from 2007 to 2013, Journal of Geophysical Research: Atmospheres, 119, 6128–6139, https://doi.org/10.1002/2014jd021500, 2014.

Xue, Z., Kuze, H., and Irie, H.: Retrieval of aerosol optical thickness with custom aerosol model using SKYNET data over the Chiba area, Atmosphere (Basel)., 12, https://doi.org/10.3390/atmos12091144, 2021.